Steady-State Heat Transport and Work With a Single Artificial Atom Coupled to a Waveguide: Emission Without External Driving

Yong Lu,[1,*] Neill Lambert,[2,†] Anton Frisk Kockum,[1] Ken Funo,[2] Andreas Bengtsson,[1] Simone Gasparinetti,[1] Franco Nori,[2,3] and Per Delsing[1,‡]

[1] *Microtechnology and Nanoscience, MC2, Chalmers University of Technology, Göteborg SE-412 96, Sweden*

[2] *Theoretical Quantum Physics Laboratory, RIKEN Cluster for Pioneering Research, Wako-shi, Saitama 351-0198, Japan*

[3] *Department of Physics, The University of Michigan, Ann Arbor, Michigan 48109-1040, USA*

(Received 18 August 2021; revised 25 January 2022; accepted 16 March 2022; published 7 April 2022)

We observe the continuous emission of photons into a waveguide from a superconducting qubit without the application of an external drive. To explain this counterintuitive observation, we build a two-bath model where the qubit couples simultaneously to a cold bath (the waveguide) and a hot bath (a secondary environment). Our results show that the thermal-photon occupation of the hot bath is up to 0.14 photons, 35 times larger than the cold waveguide, leading to nonequilibrium heat transport with a power of up to 132 zW, as estimated from the qubit emission spectrum. By adding more isolation between the sample output and the first cold amplifier in the output line, the heat transport is strongly suppressed. Our interpretation is that the hot bath may arise from active two-level systems being excited by noise from the output line, and that the qubit coherence can be improved significantly by suppressing this noise. We also apply a coherent drive, and use the waveguide to measure thermodynamic work and heat, suggesting waveguide spectroscopy is a useful means to study quantum heat engines and refrigerators. Finally, based on the theoretical model, we propose how a similar setup can be used as a noise spectrometer which provides a solution for calibrating the background noise of hybrid quantum systems.

DOI: 10.1103/PRXQuantum.3.020305

I. INTRODUCTION

Over the past 20 years, superconducting qubit coherence times have increased from less than 1 ns to more than 1 ms [1–4]. Many studies have shown that such coherence times are limited by two-level systems (TLSs) [5–7] and that quasiparticles can also contribute [8–11]. Moreover, excessive thermal population of a qubit, arising from nonequilibrium quasiparticles, has been observed extensively, with effective temperatures in the range 30–200 mK [12–14]. More recently, ionizing radiation due to high-energy cosmic rays and radioactive decay has been shown to reduce qubit coherence [15–17]. Therefore, isolating superconducting qubits from all possible sources of noise will be crucial for realizing fault-tolerant superconducting quantum computers [16,18,19].

In addition, in the field of quantum thermodynamics, alongside the study of quantum heat engines [20–23] and refrigerators [24,25], steady-state heat flows, mediated by phonons or photons, have been investigated in solid-state circuits [26], nanostructures [27,28], and superconducting circuits [29,30]. More recently, the potential for significant quantum effects was introduced into such studies in the form of a superconducting qubit coupled to cavities [31–35]. In particular, a heat valve for energy transfer between two artificial heat baths constructed from resonators has been realized, where the transferred power was obtained indirectly from the temperature difference between the two baths which is measured by thermometers [34,36]. The direct coupling of a qubit to a waveguide, a setting known as quantum electrodynamics (QED) [37,38] has been suggested as a platform for studies in thermodynamics [39], but has not yet been extensively explored experimentally.

Moreover, even though numerous studies in circuit QED imply the presence of nonequilibrium processes (i.e., multiple environments at different temperatures), often due to quasiparticles [8–11], experimental results directly demonstrating and characterizing intrinsic nonequilibrium

*kdluyong@outlook.com
†nwlambert@gmail.com
‡per.delsing@chalmers.se

processes are lacking. Waveguide QED, in particular, is promising for analyzing nonequilibrium processes as it avoids the problem inherent in circuit QED for such studies, where the resonator, far detuned from the qubit frequency, may filter out the noise mechanism that we are interested in.

In general, in contact with a single environment, and without driving, a quantum system reaches equilibrium with its environment after a long cooling time, and in this steady state there should be no net heat flow from the system to the environment. However, in this work, even though our quantum system, consisting of a superconducting qubit coupled to a waveguide (which can be regarded as an continuous many-mode environment), *was cooled for 1 month* at the 10 mK stage of a dilution refrigerator, *we nevertheless observed continuous steady-state nonequilibrium emission from the qubit into the waveguide.* We attribute this effect to thermal excitation of the qubit by an additional intrinsic hot environment. The qubit we use was intentionally engineered to have a small decay rate into the waveguide, so that the thermal spectrum from the qubit emission due to the additional hot bath is observable. By the use of a theoretical model, we characterize this hot environment and investigate its potential origin. We also show how the qubit emission spectrum and reflectivity can be used to measure the heat and work rates (the latter in the presence of a coherent drive). Finally, based on our analysis of the nonequilibrium process in our experiment, we propose a noise spectrometer operating in the quantum regime which would enable us to investigate the environment noise over a broad frequency range.

II. SYSTEM AND MODEL

To model our experiment, we introduce a two-bath model where the qubit is simultaneously coupled to a cold (radiative) waveguide bath and a hot auxiliary (nonradiative) environment. Thus, "radiative" refers to energy exchanged with the waveguide, which is observable at the waveguide output, and "nonradiative" refers to the fact that energy exchanged with the auxiliary environment that is not directly observable. We also include a coherent drive, at frequency ω_p, through the waveguide in the system. Thus, we have a qubit and two bosonic environments described by the Hamiltonian

$$H = H_q + H_r + H_n \tag{1}$$

with

$$\frac{H_q}{\hbar} = -\frac{\Delta}{2}\sigma_z + \frac{\Omega}{2}\sigma_x, \tag{2}$$

where the qubit Hamiltonian is in the rotating frame with $\Delta = \omega_p - \omega_{01}$ and Ω as the probe strength. The radiative (waveguide) Hamiltonian H_r and the nonradiative bath Hamiltonian H_n, including couplings to the qubit (under the rotating-wave approximation), are given by

$$\frac{H_i}{\hbar} = \sum_k \omega_{k,i} a_{k,i}^\dagger a_{k,i} + \sum_k g_{k,i}\left(\sigma_- a_{k,i}^\dagger + \sigma_+ a_{k,i}\right), \tag{3}$$

where $g_{k,i}$ is the coupling strength to mode k in environment $i \in \{r, n\}$ at frequency $\omega_{k,i}$, $a_{k,i}(a_{k,i}^\dagger)$ is the corresponding annihilation (creation) operator of the mode, and σ_- (σ_+) is the lowering (raising) operator of the qubit. Hereafter, we treat both environments under the standard Born-Markov secular (BMS) approximations [40], and use this model to fit the single-tone spectroscopy and power spectrum. Under the BMS approximation (Appendix D), we define Γ_r and Γ_n as the radiative and the nonradiative decay rates, respectively, and n_r and n_n as the thermal occupations at temperatures T_r and T_n, respectively, for the two baths. A corresponding explanatory diagram is shown in Fig. 1(a), where we also illustrate that the hot bath is potentially from TLSs excited by high-frequency noise from the waveguide via a nonlinear process, as discussed further in the following.

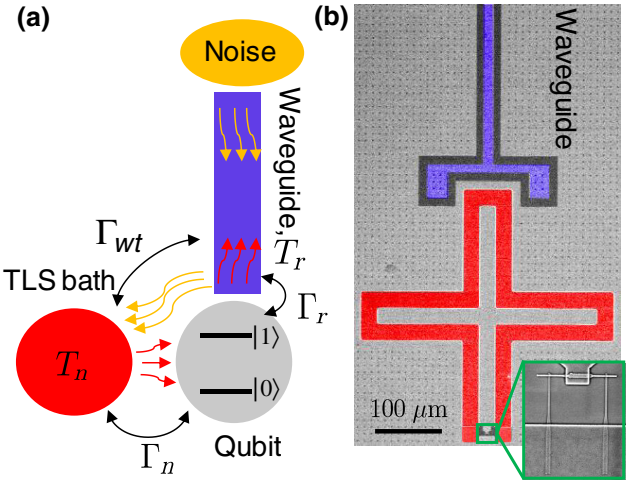

FIG. 1. Sketch of the experimental setup. (a) Schematic showing how the two-level artificial atom ($|0\rangle$ and $|1\rangle$ are the corresponding ground and excited states of the atom) absorbs energy from the hot TLS bath surrounding the atom, where the hot bath is heated by high-frequency noise from the waveguide with an unknown coupling strength between the bath and the waveguide Γ_{wt} (yellow arrows). Therefore, the excited atom emits photons to the cold waveguide (red arrows). We have Γ_r and Γ_n as the emission rates of the atom into the waveguide and the nonradiative bath, respectively. (b) False-color micrograph of the superconducting circuit realizing the setup in (a): a transmon qubit consisting of a cross-shaped superconducting island shunted by a superconducting quantum interference device (SQUID) capacitively coupled to a microwave coplanar waveguide (blue). The inset shows a close-up of the SQUID. Further details on the measurement setup are given in Appendix A.

Our device is a frequency-tunable transmon-type artificial atom [41] coupled to a one-dimensional (1D) semi-infinite waveguide, terminated by an open end, acting as a mirror in Fig. 1(b) [42–44]. We operate the qubit at the 10 mK stage of the mixing chamber of the dilution refrigerator at its maximum frequency $\omega_{01}/2\pi \approx 5.5$ GHz, where the qubit is flux-insensitive to first order, thus minimizing the pure dephasing rate.

III. QUBIT SPECTROSCOPY AND POWER SPECTRUM DENSITY

We first characterize our qubit by single-tone spectroscopy where we send a weak coherent tone to the qubit ($\Omega \ll \Gamma_r$) and then measure the coherent reflection coefficient r. Sweeping the probe frequency across the resonance of the qubit we observe that the reflection coefficient shows a dip in the amplitude [Fig. 2(a)] and a π phase shift [Fig. 2(b)]. According to input-output theory (Appendix E) with two baths under a weak probe, the reflection coefficient is

$$r = 1 - i\Gamma_r \frac{(1 - 2\Gamma_+/\Gamma_1)}{\Delta + i\Gamma_2}, \tag{4}$$

where $\Gamma_+ = n_n\Gamma_n + n_r\Gamma_r$, $\Gamma_1 = (1 + 2n_n)\Gamma_n + (1 + 2n_r)\Gamma_r$, and $\Gamma_2 = \Gamma_1/2 + \Gamma_\phi$. The pure dephasing rate Γ_ϕ can also be affected by the thermal excitation of the third level of the transmon (Appendix H). By using Eq. (4), we calculate the theoretical solid curves with $\Gamma_r(1 - 2\Gamma_+/\Gamma_1)/2\pi = 214$ kHz and $\Gamma_2/2\pi = 147$ kHz shown in Fig. 2.

Without sending any signal from room temperature to the sample, we observe a power spectral density (PSD) emitted from the qubit into the waveguide, shown as blue dots in Fig. 3(a) (more measurement details are presented in Appendix A). The Lorentzian shape centered at the qubit frequency indicates that the environment surrounding the qubit is hotter than the waveguide, and is causing heat flow into the waveguide through the qubit. In order to justify this statement, and fit the data, we use standard input-output theory for the output of the transmission line $b_{\rm out}(t) = b_{\rm in}(t) - i\sqrt{\Gamma_r}\sigma_-(t)$, where $b_{\rm in}(t) = f_{\rm in}(t) + \Omega/2\sqrt{\Gamma_1}$ includes thermal noise $f_{\rm in}(t)$ and the coherent drive $\Omega/2\sqrt{\Gamma_1}$, for the cases when such applied. It is necessary to take into account the fact that the thermal input $f_{\rm in}(t)$ to the waveguide can become correlated with the qubit emission operator $\sigma_-(t)$ to evaluate the correct output spectrum [45], given by (Appendix G)

$$S(\omega) = \frac{\hbar\omega_{01}}{2\pi}\int_{-\infty}^{\infty} dt\, e^{-i\omega t}\langle b^\dagger_{\rm out}(t) b_{\rm out}(t')\rangle_{(t'\to\infty)} \tag{5}$$

with

$$\begin{aligned}\langle b^\dagger_{\rm out}(t) b_{\rm out}(t')\rangle &= \Gamma_r\,(n_r + 1)\,\langle\sigma_+(t)\sigma_-(t')\rangle \\ &\quad - \Gamma_r n_r\langle\sigma_-(t')\sigma_+(t)\rangle + \langle f^\dagger_{\rm in}(t) f_{\rm in}(t')\rangle \\ &\quad - \frac{i\Omega^*}{2}\langle\sigma_-(t')\rangle + \frac{i\Omega}{2}\langle\sigma_+(t)\rangle + \frac{|\Omega|^2}{4\Gamma_r}.\end{aligned} \tag{6}$$

This expression is easily generalized to include more levels within the artificial atom. Importantly, if we define the Fourier transforms of the first two terms of Eq. (6), $s^+_q(\omega) = \int_{-\infty}^{\infty} dt\,\langle\sigma_+(t)\sigma_-(t')\rangle e^{-i\omega t}$ and $s^-_q(\omega) = \int_{-\infty}^{\infty} dt\,\langle\sigma_-(t')\sigma_+(t)\rangle e^{-i\omega t}$, then the limited detailed balance that arises for a qubit coupled to a single BMS environment, e.g., the waveguide, tells us that $s^-_q(\omega) = e^{\beta_r\omega_{01}} s^+_q(\omega)$, where $\beta_r = 1/k_B T_r$, and k_B is the Boltzmann constant. Hence, in equilibrium situations (no drive and no additional environment H_n), the first two terms in Eq. (6) cancel, resulting in $S(\omega) = 0$.

Explicitly evaluating the correlation functions for the qubit using our two-bath master equation [omitting both delta-function coherent contributions [46] and the background thermal black-body spectrum of the transmission line in Eq. (6)], we find the thermal spectral density output ($\Omega = 0$) is given by

$$S_{\rm th}(\omega) = \hbar\omega_{01}\frac{\Gamma_r}{2\pi}\frac{2\Gamma_2\Gamma_n\Delta n/\Gamma_1}{\delta\omega_{01}^2 + \Gamma_2^2}, \tag{7}$$

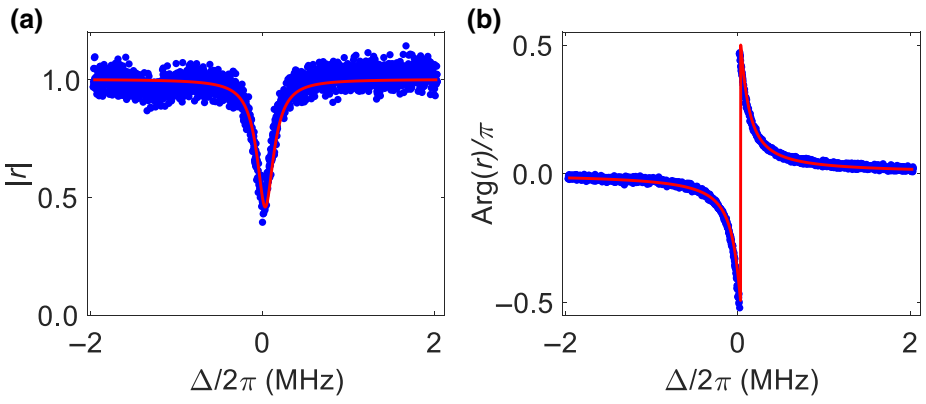

FIG. 2. Weak-power spectroscopy under a coherent drive: (a) magnitude and (b) phase response of the reflection coefficient r as a function of the probe detuning. Blue dots are the experimental data with the red solid curves calculated from Eq. (4).

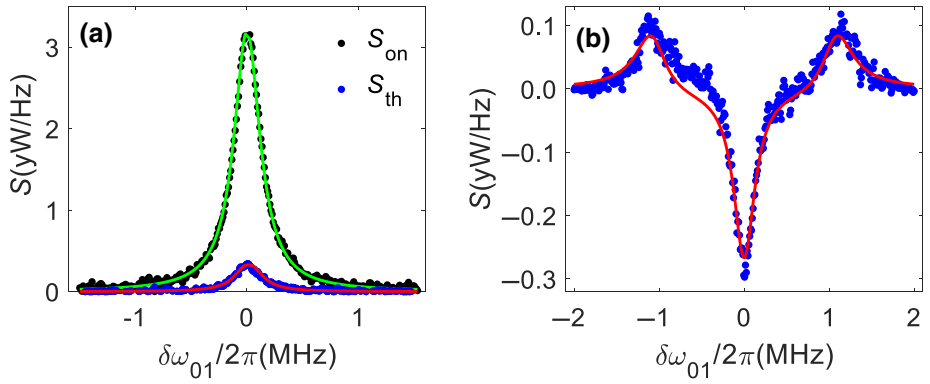

FIG. 3. Thermal spectrum. (a) Power spectral density (PSD) of the output field where the results with and without a strong drive are S_{on} and S_{th}, respectively. Units are yW/Hz = 10^{-24} W/Hz and $S = 2\pi S(\omega)$. The solid curves are the corresponding fits to Eqs. (7) and (8). The Rabi frequency used for S_{on} on the $|0\rangle \leftrightarrow |1\rangle$ transition is $\Omega/2\pi \approx 8.8$ MHz. (b) PSD from Autler-Townes splitting. The solid curve is calculated from theory. In both (a) and (b), dots are from the experimental data. The Rabi frequency used for the drive on the $|1\rangle \leftrightarrow |2\rangle$ transition is $\Omega/2\pi \approx 1.5$ MHz. Note that the PSD in (a) is subtracted by the background when tuning the qubit frequency away through the external magnetic flux, whereas in (b) the PSD is the difference between the thermal spectra with and without the drive on the $|1\rangle \leftrightarrow |2\rangle$ transition.

where $\Delta n = n_n - n_r$ and $\delta\omega_{01} = \omega - \omega_{01}$. In Eq. (7), we find that $S_{th}(\omega) = 0$ if $n_n = n_r$, as expected from detailed balance. Without the additional nonradiative bath to thermally excite the qubit, we would not observe a thermal response (even in the presence of thermal input to the transmission line). As shown in Fig. 3(a), $S_{th}(\omega) \neq 0$ in the experiment, which implies that the waveguide and the bosonic bath surrounding the qubit are not in equilibrium. Fitting Eq. (7) to the data in Fig. 3(a) gives $\Gamma_r\Gamma_n\Delta n/(2\pi\Gamma_1) = 5.6 \pm 0.2$ kHz corresponding to a transported power $\int_{-\infty}^{\infty} S_{th}(\omega)d\omega = 132 \pm 5$ zW with the given Γ_2 value from the reflection-coefficient measurement. We note that in the on-resonance case with $\Gamma_r \gg \Gamma_n, \Gamma_\phi$, Eq. (7) becomes $S_{th}(\omega) \approx 2\hbar\omega_{01}\Gamma_n\Delta n/(\pi\Gamma_r)$. Therefore, the value of $S_{th}(\omega)$ will be suppressed when Γ_r is much larger than Γ_n, making it difficult to measure the thermal spectrum.

We also send a strong drive on resonance with the qubit ($\Omega/2\pi \approx 8.8$ MHz $\gg \Gamma_1$), where such a large Rabi frequency ensures that there is no overlap between the sidebands and the center of the Mollow-triplet PSD [47,48]. For the middle peak from the elastic scattering, we have

$$S_{on}(\omega) = \hbar\omega_{01}\frac{\Gamma_r}{2\pi}\frac{\Gamma_2/2}{\delta\omega_{01}^2 + \Gamma_2^2}. \tag{8}$$

By fitting the data with the drive on [black dots in Fig. 3(a)], we obtain $\Gamma_r/2\pi = 227 \pm 4$ kHz and $\Gamma_2/2\pi = 143 \pm 4$ kHz. Compared with Eq. (7), the height of this spectrum is mostly independent of the thermal occupation difference Δn, due to the saturation of the first excited state.

IV. HEAT TRANSPORT AND WORK

Another straightforward way to evaluate the heat transport between the two baths is to measure the lost power P_{loss} due to the nonradiative decay. Shown as black in Fig. 4(a), we find that when the coherent drive is weak, the thermal noise dominates the qubit dynamics. Therefore, the qubit absorbs photons from the hot bath and then decays into the cold waveguide with a higher probability compared with the overall emission back into the hot bath, resulting in a negative lost power. When we increase the photon-flux occupation in the waveguide by increasing the drive intensity, the absolute value of P_{loss} is reduced. At $\Omega_{Rabi}/2\pi \approx 95$ kHz, we see that equilibrium is reached, with zero lost power. However, beyond this value, the waveguide occupation becomes larger than the nonradiative environment. Thus, the qubit is excited by the photons in the waveguide and then dissipates into both environments via nonradiative decay. By increasing the drive intensity further, the qubit is saturated, with the population reaching the maximum value of 0.5 in the steady state. Therefore, $P_{loss} = P_{in} - P_{scatter} \approx \hbar\omega_{01}(\Gamma_n/2)$ where $P_{scatter}$ includes both incoherent and coherent scattering from the qubit and the mirror. Theoretically, the lost power is given by

$$\begin{aligned} P_{loss} &= \hbar\omega_{01}(\langle b_{in}^\dagger b_{in}\rangle - \langle b_{out}^\dagger b_{out}\rangle) \\ &= \hbar\omega_{01}\frac{\Gamma_n}{2}\frac{\Omega^2 - 2\Gamma_2\Gamma_r\Delta n}{\Omega^2 + \Gamma_2\Gamma_1}. \end{aligned} \tag{9}$$

By fitting Eq. (9) to the data using the values of Γ_2 and Γ_r extracted from the fit of Eq. (8), with Ω calibrated by the Mollow-triplet (black solid curve), we obtain $\Gamma_n/2\pi = 55 \pm 3$ kHz with $\Delta n = 0.135$ photons

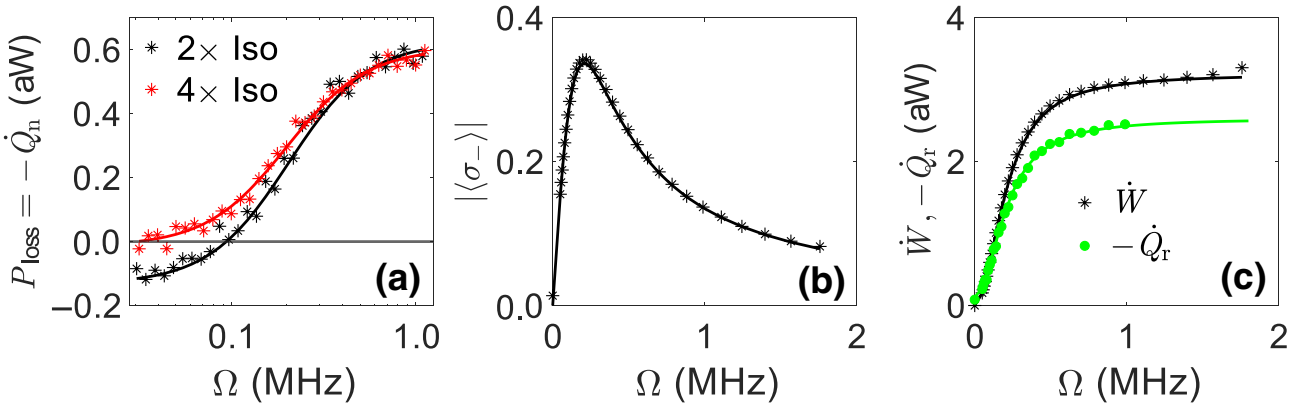

FIG. 4. Power loss, work, and heat. (a) The lost power $P_{\rm loss}$ as a function of the Rabi frequency (Ω) of the drive with two and four isolators. (b) The magnitude of the qubit emission as a function of Ω of the drive with two isolators. (c) Work ($\dot{W}$) performed and heat ($\dot{Q}$) generated by the drive as a function of Ω. In all panels, the stars are the experimental data and the solid curves are from theory, where the green dots in (c) are from the difference between the values of the black stars in (c) and (a) according to $\dot{Q}_r = P_{\rm loss} - \dot{W}$.

and $\Gamma_1/2\pi = 299$ kHz. The transported power from the hot bath is about 132 zW which is consistent with the integral of the thermal spectrum in Fig. 3(a). Without an external drive ($\Omega = 0$) with a large value of Γ_r, Eq. (9) becomes $P_{\rm loss} \approx \hbar\omega_{01}\Gamma_n$, which is independent of the radiative decay, enabling the possibility of observing the heat flow even when the radiative decay rate is much larger than the nonradiative decay rate.

To obtain the temperature of the waveguide and the bath separately, we combine the value of Δn with the result from the reflection-coefficient measurement where we can obtain the thermal population of the qubit $\rho_{11}^{\rm th} = \Gamma_+/\Gamma_1 \approx 2.86\%$ from the extracted parameters. Consequently, we obtain $n_r \approx 0.004$, $n_q \approx 0.03$ and $n_n \approx 0.139$ corresponding to $T_r \approx 50$ mK for the cold waveguide, $T_q \approx 78$ mK for the qubit and $T_n \approx 131$ mK for the hot bath, respectively. Therefore, we can obtain the value of $\Gamma_1 = (1 + 2n_n)\Gamma_n + (1 + 2n_r)\Gamma_r \approx 2\pi \times 299 \pm 7$ kHz which is very close to $2\Gamma_2$, indicating that the pure dephasing rate Γ_ϕ is negligible at the flux sweet spot.

In order to make sure that the environment is not affected when changing the external magnetic flux to tune the qubit away from its maximum frequency, we send a strong drive on the transition between the second and third levels of the transmon, inducing an Autler-Townes splitting [49]. Then, we obtain the PSD subtracted from the reference with the drive off, where we observe two peaks and one dip [blue in Fig. 3(b)]. The two peaks are the thermal spectra from the thermal emission of the dressed states when a strong drive is applied on the $|1\rangle \leftrightarrow |2\rangle$ transition. The distance between these two peaks are twice of the corresponding Rabi frequency: $2\Omega \approx 2\pi \times 3.0$ MHz. When the drive is off, as we discussed, we have a thermal spectrum $S_{\rm th}$ at the undressed qubit frequency. Importantly, we have a dip at that frequency when we subtract the data with the drive off from the data with the drive on. We find that the numerical result from the master equation [red in Fig. 3(b)] matches well the data [blue in Fig. 3(b)] with parameters $\Gamma_r/2\pi = 227$ kHz, $\Gamma_n/2\pi = 55$ kHz, and $\Delta n = 0.135$. These parameters agree fully with those extracted from the power-loss measurements.

When we drive the qubit, the external field is doing work on this single-atom quantum system. Defining $H_0 = (\hbar\omega_{01}/2)\sigma_z$ as the bare Hamiltonian which measures the internal energy of the qubit, and $H_1 = (\hbar\Omega/2)\sigma_x$ as the drive Hamiltonian, the work performed on the qubit by the coherent drive can be extracted [33,50] and it is defined as (see also Refs. [51,52] for an alternative definition)

$$\dot{W} = \mathrm{Tr}\{-i[H_0, H_1]\rho\} = \frac{\hbar\Omega}{2}\langle\sigma_y\rangle = \hbar\Omega\Re[i\langle\sigma_-\rangle]. \quad (10)$$

Therefore, the work $\dot{W}$ only depends on the qubit coherent emission $\langle\sigma_-\rangle$ with $\langle\sigma_-\rangle = i(\langle b_{\rm out}\rangle - \langle b_{\rm in}\rangle)/\sqrt{\Gamma_r}$. In particular, when the drive is on resonance with the qubit [see Eq. (D9)], it leads to $\dot{W} = i\hbar\Omega\langle\sigma_-\rangle = \hbar\Omega|\langle\sigma_-\rangle|$. We obtain $\langle\sigma_-\rangle$ from the values of $\langle b_{\rm out}\rangle$ and $\langle b_{\rm in}\rangle$ which are measured with and without the qubit by tuning the qubit frequency. The results match well with theory [black in Figs. 4(b) and 4(c)], where the work increases with the drive intensity and then saturates around 3.2 aW due to the saturation of the qubit.

In addition to the work, the heat from the waveguide and the hot bath can be derived from $\dot{Q} = \mathrm{Tr}\{H_0\mathcal{L}[\rho]\} = \dot{Q}_r + \dot{Q}_n$, where $\mathcal{L}[\rho]$ is the dissipative part of the Liouvillian for the interaction with both baths (Appendix D), and $\dot{Q}_i = \hbar\omega_{01}(\Gamma_i n_i\langle\sigma_-\sigma_+\rangle - \Gamma_i(n_i + 1)\langle\sigma_+\sigma_-\rangle)$ $i \in \{n, r\}$. In particular, we find from Eq. (6) that $\dot{Q}_r = P_{\rm loss} - \dot{W}$ [blue in Fig. 4(c)], where the negative values of $\dot{Q}_r$ means that the waveguide is heated up due to the qubit emission. Interestingly, when the drive is off ($\dot{W} = 0$), and in the steady state (the change of the internal energy of the qubit $\dot{U} = \mathrm{Tr}\{H_0\partial_t\rho(t)\} = 0$), the first law of thermodynamics $\dot{Q}_r + \dot{Q}_n + \dot{W} = \dot{U}$ implies that we have $\dot{Q}_n = -\dot{Q}_r$,

indicating the heat exchange between these two baths, consistent with what we observed.

In a separate cooldown, we observe that improving the isolation between the sample and the first amplifier in our chain (Appendix A) leads to a strong reduction in the nonequilibrium heat flow, and a reduced thermal population of the qubit [red stars in Fig. 4(a)]. This observation suggests that the temperature of the nonradiative environment has been reduced, with $\Gamma_n/2\pi = 53 \pm 4$ kHz, and that the two baths are in thermal equilibrium without external drive. Therefore, we have a reduced thermal population of our qubit: $\rho_{11}^{\text{th}} \approx 0.4\%$. It is possible that noise from the high-mobility electron transistor (HEMT) amplifier at the 4K stage induces quasiparticles [53,54] or active TLSs [11,55] where TLSs are typically located in the dielectrics of the surfaces of the substrate and the Josephson junctions, and possibly in the tunnel barrier of the Josephson junctions.

Quasiparticles may, in principle, be generated from stray thermal noise propagating to the sample from the output line. These "hot" quasiparticles with energy higher than $\Delta_g + \hbar\omega_{01}$ could excite the qubit [12,53,54], where Δ_g is the superconducting gap. However, from the thermal population of our qubit $\rho_{11}^{\text{th}} \approx 2.86\%$, we can infer that the quasiparticle-induced nonradiative decay rate should be $\Gamma_{\text{QP}}/2\pi \approx 84\,\text{kHz} > \Gamma_n$ (see Appendix B), in conflict with our observations. Moreover, if the excitation was dominated by the quasiparticles, the value of Γ_n should decrease when we decrease the temperature of the hot bath which is not the case in our experiment. Conversely, we do not see a substantial increase either, as might be expected for a purely TLS bath (see Appendix B). Thus, we believe our hot bath is primarily from excited TLSs. In addition, we have measured the total attenuation from the isolators and the filters between the amplifier and the sample [Fig. 6(a)]. According to the attenuation, we find that at the qubit frequency ($\omega_{01}/2\pi \approx 5.5$ GHz), the reduced noise temperature is 34 mK [Fig. 6(b)], less than the measured qubit temperature $T_q = 78$ mK. This implies that the hot bath is activated by noise at higher frequencies. In Ref. [56] it is shown that the first transistor in the amplifier is overheated to temperatures of tens of kelvin which will generate high-frequency noise up to several hundred gigahertz. At those frequencies, filters and isolators may become more transparent and this is the likely source of radiation that heats up the bath of TLSs (see Appendix C for a detailed discussion). We also point out that our model makes it possible to study the energy exchange between "hot" quasiparticles and a cold waveguide, if the waveguide is cold enough (see Appendix B).

V. NOISE SPECTROMETER

Based on the model we developed here, we propose that our study also enables the construction of a practical noise spectrometer. In detail, we could engineer two waveguide channels coupled to the qubit, similar to the setup in Refs. [57,58], but with equally strong coupling on both sides with $\Gamma_1 = 2\Gamma_r$ ($\Gamma_r \gg \Gamma_n$). One channel, acting as a probe, could be used for inputting noise while the other, acting as a detector, is for measuring the noise PSD. In this setup, the noise can be very well isolated from the detection channel because the direct capacitive coupling between the probe and detection channels can be designed to be extremely small [57,58].

In this scenario, the thermal spectral density in Eq. (7) becomes

$$S_{\text{th}}(\omega) = \hbar\omega_{01}\frac{\Gamma_r}{2\pi}\frac{\Gamma_2\Delta n}{\delta\omega_{01}^2 + \Gamma_2^2}, \tag{11}$$

where $\Delta n = n_{\text{th}} - n_r$, with n_{th} (n_r), the temperature of the probe (detection) channel. We note that Eq. (8) is still valid. Thus, we can evaluate the value of Δn at the qubit frequency according to $\Delta n = S_{\text{th}}(\omega)/2S_{\text{on}}(\omega)$ if $S_{\text{th}}(\omega)$ and $S_{\text{on}}(\omega)$ are measured. Furthermore, by taking the integral of the spectra, we have the powers $P_{\text{th}} = \hbar\omega_{01}\Gamma_r\Delta n/2$ and $P_{\text{on}} = \hbar\omega_{01}\Gamma_r/4$ for S_{th} and S_{on}, respectively. Therefore, we obtain $\Delta n = P_{\text{th}}/2P_{\text{on}}$.

Compared with measuring the whole spectra, the second method will reduce the measurement time by a factor proportional to the number of data points in the spectra. However, by observing the symmetry of the spectra, we can check whether the bandwidth of the noise is larger than Γ_r or not, which can be possible when a qubit strongly couples to some resonant TLSs [59]. Note that it is not necessary to calibrate the system gain with these two measurements. Moreover, because the method is insensitive to Γ_ϕ, this insensitivity makes the method robust against flux noise, which introduces excess dephasing when the qubit frequency is tuned away from the sweet spot. As a result, the spectrometer can be reliably operated over a broad frequency range. Combined with the reflection coefficient, we will have $r = n_{\text{th}} + n_r$, when $\Gamma_\phi \ll \Gamma_r$. Thus, we can obtain n_{th} and n_r, separately.

Compared with thermometers based on tunnel junctions [60] and a proximity Josephson junction [61], our proposal does not require additional calibration and enables the possibility to obtain the noise spectrum by sweeping the qubit frequency. Circuit-QED radiometers [25,62] have also been developed, where the bandwidth is limited by the cavity. Very recently, a thermometer based on the reflection coefficient of a qubit in front of a mirror was demonstrated [63], where it has a single bosonic bath in the waveguide, namely, $\Gamma_r \neq 0$ ($n_r \neq 0$) with $\Gamma_n = 0$ ($n_n = 0$). Compared with Ref. [63], the thermometry method suggested here, based on PSD measurements, can tolerate a higher noise background in the probe waveguide, and, unlike Ref. [63], is insensitive to the pure dephasing rate. Finally, separating the detection and probe channels can make it easier

to connect our thermometer chip directly to other hybrid quantum systems [64–67].

VI. DISCUSSION AND CONCLUSION

In summary, with the system parameters listed in Table I, we have constructed a two-bath model to explain the heat transport via a superconducting qubit. Our study indicates that the qubit excited-state population is increased up to 2.9% due to interaction with a hot environment, probably from excited TLSs, with an equivalent temperature of about 131 mK. This temperature can be reduced by adding more isolation between the sample and the output line, leading to the thermal population of our qubit being reduced by almost one order of magnitude. Our results point at the necessity of providing sufficient isolation between the sample and the HEMT amplifier to mitigate residual thermal occupation of qubits, which adversely affects state preparation in quantum computing applications [18,19].

Moreover, as presented in the master equation, the noise will increase the intrinsic qubit relaxation rate by $\Gamma_+ = n_n\Gamma_n + n_r\Gamma_r$. Thus, Γ_+ is reduced from about 9 kHz with two isolators to 1 kHz with four isolators, which is about 15% of the nonradiative decay rate. Such a large improvement will be important in circuit QED, where generally the radiative decay Γ_r is negligible and Γ_n dominates the qubit decay. Our study shows that waveguide spectroscopy may be a useful tool to understand the origin of various noise sources, which will be crucial to improve qubit coherence in future devices. More importantly, in addition to increasing the qubit coherence by reducing the number of the TLSs [5–7,55], our study implies that it is necessary to reduce the high-frequency noise away from the qubit frequency which can excite TLSs to affect the qubit state and reduce the qubit coherence.

We also emphasize that it is nontrivial to observe this nonequilibrium phenomenon because it is difficult to observe and study the heat transport we observed in our device when the nonradiative decay is very small compared with the radiative decay rate, which is typically the case in other experiments. In addition, even though one can measure the thermal population of a qubit in standard circuit QED, which can allow us to extract one bath temperature or the sum of temperatures of several baths, it is difficult to separate each bath temperature in the multibath case. Here, by measuring the power spectrum and the reflection coefficient, we can obtain information on both bath temperatures. Note that our model can be easily extended to a multibath case by adding more coupling channels between the baths and the qubit.

We also showed that, under strong drive, we can use the waveguide to measure work and heat rates. While our quantum system is operating in a regime where the drive only increases the heat rate to both environments, having direct access to the work, from measuring the coherent output, and the heat, from the power loss, is a powerful tool for the future study of regimes where useful tasks such as cooling or work extraction can be performed.

Finally, from the two-bath model, we developed a noise spectrometer which can be regarded as a quantum thermometer. As this thermometer works through the power spectrum density of the qubit emission, it enables the possibility to investigate not only the bath temperature at different frequencies but also whether the qubit is strongly coupled to some TLSs, which may give rise to asymmetry and side peaks in the spectrum [59].

TABLE I. Summary of the system parameters including different qubit decay rates and temperatures of the qubit, waveguide and the hot bath.

$\Gamma_r/2\pi$ (kHz)	$\Gamma_n/2\pi$ (kHz)	$\Gamma_1/2\pi$ (kHz)	$\Gamma_2/2\pi$ (kHz)	T_q (mK)	T_r (mK)	T_n (mK)
227 ± 4	55 ± 3	299 ± 7	143 ± 4	78	50	131

ACKNOWLEDGMENTS

We acknowledge fruitful discussions with Shahnawaz Ahmed, Dr. Jonathan Burnett, and Dr. Xinyuan You. We also thank Dr. Niklas Wadefalk and Dr. Sumedh Mahashabde for useful discussions about the HEMT amplifiers. Numerical modeling was performed using the QuTiP library [68]. N.L. acknowledges partial support from JST PRESTO through Grant No. JPMJPR18GC. F.N. is supported in part by: NTT Research, Japan Science and Technology Agency (JST) (via the Q-LEAP program, Moonshot R&D Grant No. JPMJMS2061, and the CREST Grant No. JPMJCR1676), Japan Society for the Promotion of Science (JSPS) (via the KAKENHI Grant No. JP20H00134 and the JSPS-RFBR Grant No. JPJSBP120194828), Army Research Office (ARO) (Grant No. W911NF-18-1-0358), and Asian Office of Aerospace Research and Development (AOARD) (via Grant No. FA2386-20-1-4069). F.N. and N.L. acknowledge the Foundational Questions Institute Fund (FQXi) via Grant No. FQXi-IAF19-06. We acknowledge the use of the Nanofabrication Laboratory (NFL) at Chalmers. Y.L., A.F.K., S.G., and P.D. were supported by the Knut and Alice Wallenberg Foundation through the Wallenberg Center for Quantum Technology (WACQT). Y.L. and P.D. are supported by the Swedish Research Council [VR Rådsprof (5920793)].

APPENDIX A: MEASUREMENT SETUP

Figure 5 shows our measurement setup, where a transmon qubit is weakly coupled to a 1D semi-infinite transmission line. To measure the reflection coefficient, a vector network analyzer (VNA, not shown)

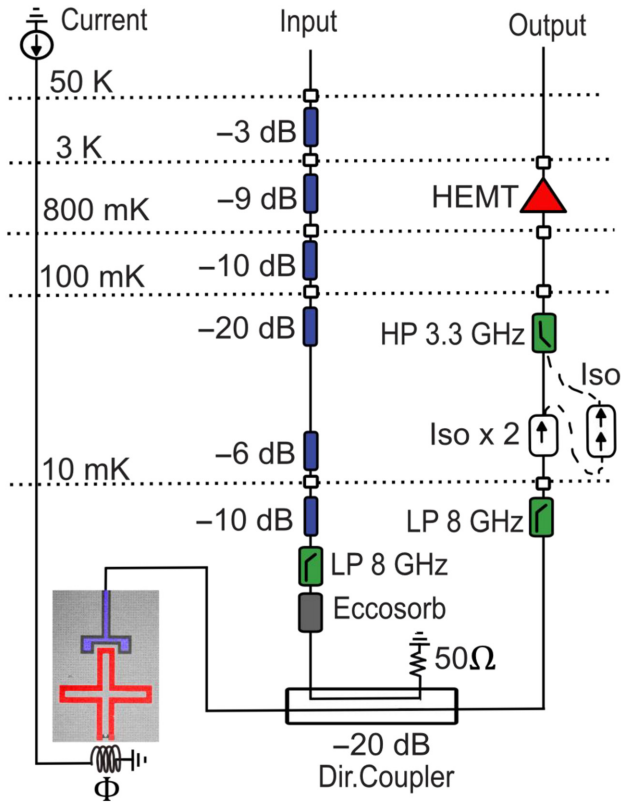

FIG. 5. Experimental setup. Setup inside the dilution refrigerator. The signal from the input port is attenuated and fed into the waveguide through a low-pass filter (LP), Eccosorb, and a −20 dB directional coupler. After interacting with the transmon, the signal from the sample goes through the directional coupler again, passes another LP, two isolators (Iso), and a high-pass filter with amplification from a HEMT amplifier (LNA056 from Low Noise Factory). The qubit frequency can be changed by sending a current to the magnetic flux coil to generate an external magnetic flux Φ through the SQUID. The isolators are from Low Noise Factory where we used two single-junction isolators (LNF-ISC4-8A) when we observed the hot bath. To suppress the noise from the HEMT amplifier, instead of connecting the two isolators to the HP filter, we add a two-junction isolator (LNF-ISISC4-8A) with 40 dB isolation (dashed line). All the isolators are mounted at the 10 mK stage.

generates coherent continuous microwaves which are sent into the input line. This signal is attenuated, passes through a 20 dB directional coupler, and then reaches the qubit. After the interaction with the qubit, the electrical field is reflected back, and passes filters, isolators, and a HEMT amplifier. Finally, it goes back to the VNA to obtain the reflection coefficient with some room-temperature amplifiers.

To measure the PSD from the thermal noise, turning off the VNA, we use a digitizer to measure the voltage from the output port in the time domain where the sampling rate is 3 MHz and 4 MHz for Figs. 3(a) and 3(b), respectively. Such rates are large enough to capture the signal around the qubit in the frequency domain. The measured voltage is then normalized to the system gain based on the Mollow-triplet spectrum [47]. Afterwards, we calculate the PSD according to the Welch method [69], where the background noise is subtracted by the reference found by tuning the qubit frequency away using the external magnetic flux. Experimentally, in order to remove the background and the gain drift, we first measure the PSD for 1 s with the drive either on or off, as required. After that, we tune the qubit away by changing the external flux and repeat the measurement to obtain the background reference. Finally, we just take the difference between these two measurements to obtain either $S_{\rm on}$ or $S_{\rm off}$, if the drive was on or off, respectively.

APPENDIX B: QUASIPARTICLES AND TWO-LEVEL SYSTEMS

In addition to the hot bath we discussed, nonequilibrium quasiparticles could also excite and decay the qubit with rates $\Gamma_\uparrow$ and $\Gamma_\downarrow$, respectively. Therefore, we add two additional dissipators ($\Gamma_\downarrow \mathcal{D}[\sigma_-]\rho$ and $\Gamma_\uparrow \mathcal{D}[\sigma_+]\rho$) into the master equation used for our model (Appendix D). By solving the master equation without external drive, we obtain the lost power, which contains the effects from both the hot bath and quasiparticles as

$$\frac{P_{\rm loss}}{\hbar\omega_{01}} = \frac{\Gamma_r\Gamma_n(n_r - n_n) - \Gamma_r[(n_r+1)\Gamma_\uparrow - n_r\Gamma_\downarrow]}{\Gamma_1 + \Gamma_\uparrow + \Gamma_\downarrow}. \quad \text{(B1)}$$

When $\Gamma_n = 0$ and $n_r = 0$, the qubit population due to the nonequilibrium quasiparticles is $\rho_{11}^{\rm QP} = \frac{\Gamma_\uparrow}{\Gamma_\uparrow+\Gamma_\downarrow}$. Experimentally, we can increase the capacitive coupling between the waveguide and the qubit in order to make the nonradiative decay negligible ($\Gamma_r \gg \Gamma_n$). By suppressing the noise from the output line, as we did in the main text, we have $n_r \approx n_n$. In these conditions, the lost power is mainly from the quasiparticles. Depending on the value of the waveguide thermal-photon occupation, we have three regimes: if $n_r > \Gamma_\uparrow/(\Gamma_\downarrow - \Gamma_\uparrow)$, $P_{\rm loss} > 0$, the qubit is thermally excited and prefers to be dissipated due to the quasiparticle tunneling through the Josephson junction; if $n_r < \Gamma_\uparrow/(\Gamma_\downarrow - \Gamma_\uparrow)$, $P_{\rm loss} < 0$, the quasiparticles excite the qubit, and then the qubit emits a photon into the waveguide; if $n_r = \Gamma_\uparrow/(\Gamma_\downarrow - \Gamma_\uparrow)$, $P_{\rm loss} = 0$, we can consider the effects on the qubit from the quasiparticles and the thermal photons in the waveguide are the same.

The quasiparticle-induced excited-state population can be approximately written as [53]

$$\rho_{11}^{\rm QP} \simeq 2.17\frac{n_{\rm QP}}{n_{\rm CP}}\left(\frac{\Delta_g}{\hbar\omega_{01}}\right)^{3.65}, \quad \text{(B2)}$$

in which $n_{\rm QP}$ ($n_{\rm CP}$) is the density of all quasiparticles (Cooper pairs) and Δ_g is the superconducting energy gap.

Combining this with the quasiparticle-induced decay rate for a transmon qubit [9,53]

$$\Gamma_{\downarrow} \simeq \frac{\sqrt{2}}{R_N C}\frac{n_{\mathrm{QP}}}{n_{\mathrm{CP}}}\left(\frac{\Delta_g}{\hbar\omega_{01}}\right)^{1.5}, \tag{B3}$$

we have

$$\Gamma_{\downarrow} \simeq \frac{\sqrt{2}}{2.17 R_N C}\left(\frac{\Delta_g}{\hbar\omega_{01}}\right)^{-2.15}\cdot\rho_{11}^{\mathrm{QP}}, \tag{B4}$$

where the normal resistance of our SQUID is $R_N \approx 6.3$ kΩ, the total capacitance of the qubit is $C = 78$ fF and $\Delta_g = 170$ μeV for aluminum. By assuming that our thermal population is solely from the quasiparticles, i.e., $\rho_{11}^{\mathrm{QP}} = \rho_{11}^{\mathrm{th}} \approx 2.86\%$, we have $\Gamma_{\downarrow}/2\pi \approx 87$ kHz. Therefore, we have $\Gamma_{\uparrow} \approx \rho_{11}^{\mathrm{QP}}\Gamma_{\downarrow} \approx 2\pi \times 3$ kHz. Thus, the quasiparticle-induced nonradiative decay rate would be $\Gamma_{\mathrm{QP}} = \Gamma_{\downarrow} - \Gamma_{\uparrow} \approx 2\pi \times 84$ kHz $> \Gamma_n$, see the discussion in the main text.

Finally, as discussed in the main text, we do not observe any considerable decrease in Γ_n as the temperature is lowered (by the addition of isolators). Conversely, we also note that the value of Γ_n does not observably increase. If we assume that Γ_n is solely from TLSs, then, when we decrease the bath temperature from 131 to 50 mK, the value of Γ_n is expected to increase by about 10 kHz according to the relationship $\Gamma_{n,\mathrm{TLS}} = \Gamma_{n,0}\tanh(\hbar\omega_{01}/k_B T)$ [7] (see also Appendix D), where $\Gamma_{n,0}$ is the nonradiative decay rate due to TLSs at zero temperature. It may be that the high-temperature noise from the output may also generate some quasiparticles. Assuming that the noise temperature is the same as that of the TLS bath, namely, 131 mK, the corresponding quasiparticle-induced decay rate is about 8 kHz, as given by $\Gamma_{\mathrm{QP}} = \frac{\omega_{01}}{\pi}\sqrt{\frac{2\Delta_g}{\hbar\omega_{01}}}x_{\mathrm{QP}}$ with the normalized quasiparticle density $x_{\mathrm{QP}} = \frac{\sqrt{2\pi\Delta_g k_B T}}{\Delta_g}e^{-\Delta_g/k_B T}$ [9,70], and said rate would decrease as the noise temperature is lowered. In total, it is possible that we do not see a change in Γ_n after suppressing the noise because these two effects (TLS rate increasing due to less saturated TLSs, quasiparticle rate decreasing due to a lower quasiparticle density) mitigate each other, according to $\Gamma_n = \Gamma_{n,\mathrm{TLS}} + \Gamma_{\mathrm{QP}}$. Such behavior has been observed in superconducting resonators [71].

APPENDIX C: NOISE ANALYSIS

In order to investigate where the noise is from, as shown in Fig. 6(a), we measure the isolation and the transmission for two isolators, and the filters with a low-pass and high-pass filter at 77 K. We find that from 4 to 8 GHz, which is the bandwidth of the isolators, the isolation of the isolators can be up to 40 dB. Outside the bandwidth, the filters can suppress the noise well up to 20 GHz. According to the noise temperature of the HEMT amplifier from the datasheet, we can calculate the corresponding thermal photons n_{HEMT}. Therefore, the reduced noise temperature to the sample is given by [72]

$$n_{\mathrm{th}} = A(\omega)n_{\mathrm{HEMT}} + [1 - A(\omega)]n(\omega, T_{\mathrm{MX}}), \tag{C1}$$

where $A(\omega)$ is the total attenuation [black curve in Fig. 6(a)]. $n(\omega, T_{\mathrm{MX}}) = 1/[e^{\hbar\omega/(k_B T_{\mathrm{MX}})} - 1]$ is the thermal photons from the 50 Ω terminators of the two single-junction isolators, where we simply assume that the terminator has the same temperature as the mixing chamber of the dilution refrigerator, namely, $T_{\mathrm{MX}} = 10$ mK and its contribution to the total noise temperature is shown as the red curve in Fig. 6(b).

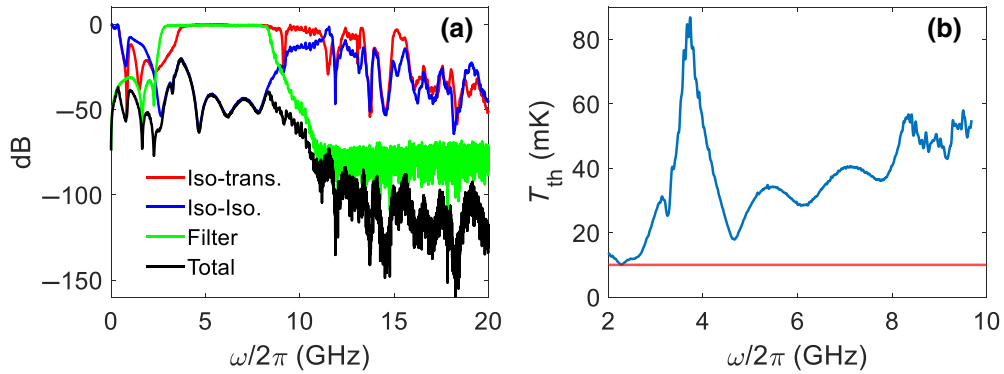

FIG. 6. Noise temperature. (a) The response of filters with a low-pass and high-pass filters and two single-junction isolators shown in Fig. 5, as a function of the input frequency ω. The data is measured by a VNA with dipping the microwave components into liquid nitrogen. Iso-trans. and Iso-Iso denote the transmission coefficient and the isolation coefficient of the two single-junction isolators, respectively. The green curve is the filters' transmission coefficient. The black curve represents the total attenuation from the filters and the isolators. (b) The corresponding effective noise temperature T_{th} reaching the sample from the HEMT amplifier after the isolators and filters (blue curve). The red curve is the noise temperature from the 50 Ω terminators of the isolators.

In Fig. 6(b), we find that the noise temperature is mainly dominated by the noise from the HEMT amplifier compared to the 50 Ω terminators. However, it is far away from the hot-bath temperature (130 mK), especially at the qubit frequency; the value is 34 mK, much lower than the actual qubit temperature ($T_q = 78$ mK). Moreover, from 10 GHz to 20 GHz, the low-pass filter will suppress the noise strongly up to 80 dB. Therefore, we suppose it is likely that the noise heating up the TLS bath is above 20 GHz. According to the datasheet, the filter can work until 40 GHz. Above that, it will have a frequency where it stops to suppress the high-frequency noise. Thus, the high-frequency noise possibly heats up the TLS bath by some nonlinear process. A possible scenario is that the TLSs are excited to metastable states that decay and emit photons over a broad frequency range, including the qubit frequency. This secondary radiation then excites the qubit, leading to a partially excited qubit that can emit radiation to the amplifier at the qubit frequency. After adding a two-junction isolator, even though the isolation at the high frequency may be not so effective, it can still attenuate the high-frequency noise, leading to a lower bath temperature as we observed in the main text.

APPENDIX D: MASTER EQUATION

The dynamics and steady state of the qubit in contact with two bosonic heat baths can be found, in the weak-coupling and Markovian approximations, by solving the equation of motion

$$\frac{\partial}{\partial t}\rho_S(t) = -\frac{i}{\hbar}[H_q, \rho(t)] + \mathcal{L}[\rho(t)], \tag{D1}$$

where

$$\begin{aligned}\mathcal{L}[\rho(t)] = &\frac{\Gamma_r}{2}(n_r+1)\,\mathcal{D}[\sigma_-]\rho + \frac{\Gamma_r}{2}n_r\mathcal{D}[\sigma_+]\rho \\ &+ \frac{\Gamma_n}{2}(n_n+1)\,\mathcal{D}[\sigma_-]\rho + \frac{\Gamma_n}{2}n_n\mathcal{D}[\sigma_+]\rho \\ &+ \frac{\Gamma_\phi}{4}\mathcal{D}[\sigma_z]\rho,\end{aligned} \tag{D2}$$

where the Lindblad operator is $\mathcal{D}[\sigma_i]\rho(t) = 2\sigma_i\rho(t)\sigma_i^\dagger - \{\sigma_i^\dagger\sigma_i, \rho(t)\}$, and the thermal occupation of the bosonic baths are given by $n_i = [\exp(\hbar\omega_{01}/k_\mathrm{B}T_i) - 1]^{-1}$, where k_B is the Boltzmann constant.

The qubit Hamiltonian is

$$\frac{H_q}{\hbar} = -\frac{\Delta}{2}\sigma_z + \frac{\Omega}{2}\sigma_x, \tag{D3}$$

where the detuning $\Delta = \omega_p - \omega_{01}$ is the energy difference between the drive at frequency ω_p and the bare qubit frequency ω_{01}.

In the above, we explicitly assume that the qubit only has two levels, and that the radiative (transmission line) and nonradiative baths are bosonic, and obey the BMS approximation. The influence of a third level is described in the following.

The second assumption, the bosonicity of the nonradiative bath, can be replaced by assuming a TLS bath. This simply changes the temperature dependence of the Lindblad operators for that bath, such that

$$\frac{\Gamma_n}{2}(n_n+1)\,\mathcal{D}[\sigma_-] \to \frac{\Gamma_n}{2}\left(\frac{1+n_n}{1+2n_n}\right)\mathcal{D}[\sigma_-], \tag{D4}$$

$$\frac{\Gamma_n}{2}(n_n)\,\mathcal{D}[\sigma_+] \to \frac{\Gamma_n}{2}\left(\frac{n_n}{1+2n_n}\right)\mathcal{D}[\sigma_+]. \tag{D5}$$

Ultimately, this implies some ambiguity in the temperature ascertained from the height of the thermal peak in the spectrum calculation. For simplicity we use that obtained from the bosonic assumption, but note that a TLS bath requires a larger temperature to produce the equivalent thermal peak in the spectrum, because $k_\mathrm{B}T_n = \hbar\omega_{01}/[\ln(1 \pm n_n) - \ln(n_n)]$, where $\pm = +$ for a bosonic bath, and $\pm = -$ for a TLS bath. For example, for the $\Delta n = 0.135$ observed in the main text we would find, assuming $n_r = 0$, $k_\mathrm{B}T_n/\hbar\omega_{01} = 0.47$ for a bosonic bath and 0.54 for a TLS one.

It is convenient to use the Heisenberg equations of motion generated by Eq. (D1) for the operators $s_1(t) = \langle\sigma_-(t)\rangle$, $s_1^*(t) = \langle\sigma_+(t)\rangle$, and $s_2(t) = \langle\sigma_+(t)\sigma_-(t)\rangle$:

$$\frac{d}{dt}\begin{pmatrix} s_1 \\ s_1^* \\ s_2 \end{pmatrix} = M\begin{pmatrix} s_1 \\ s_1^* \\ s_2 \end{pmatrix} + B, \tag{D6}$$

where

$$M = \begin{pmatrix} i\Delta - \Gamma_2 & 0 & i\Omega \\ 0 & -i\Delta - \Gamma_2 & -i\Omega^* \\ i\Omega^*/2 & -i\Omega/2 & -\Gamma_1 \end{pmatrix} \tag{D7}$$

and

$$B = \begin{pmatrix} -i\Omega/2 \\ i\Omega^*/2 \\ \Gamma_+ \end{pmatrix} \tag{D8}$$

and where, as in the main text, $\Gamma_+ = n_n\Gamma_n + n_r\Gamma_r$, $\Gamma_1 = (1+2n_n)\Gamma_n + (1+2n_r)\Gamma_r$, and $\Gamma_2 = \Gamma_\phi + \Gamma_1/2$. For the steady state $t \to \infty$ this gives

$$\langle\sigma_-(t\to\infty)\rangle = \frac{\Omega(\Gamma_1 - 2\Gamma_+)(\Delta - i\Gamma_2)}{2\Omega^2\Gamma_2 + 2(\Delta^2 + {\Gamma_2}^2)\Gamma_1} \tag{D9}$$

$$\langle\sigma_+\sigma_-(t\to\infty)\rangle = \frac{|\Omega|^2\Gamma_2 + 2\Gamma_+(\Delta^2 + {\Gamma_2}^2)}{2|\Omega|^2\Gamma_2 + 2(\Delta^2 + {\Gamma_2}^2)\Gamma_1} \tag{D10}$$

$$\langle \sigma_- \sigma_+ (t \to \infty) \rangle = \frac{|\Omega|^2 \Gamma_2 + 2\Gamma_- (\Delta^2 + {\Gamma_2}^2)}{2|\Omega|^2 \Gamma_2 + 2(\Delta^2 + {\Gamma_2}^2)\Gamma_1}, \quad \text{(D11)}$$

where in the last equation $\Gamma_- = (n_n + 1)\Gamma_n + (n_r + 1)\Gamma_r$.

APPENDIX E: REFLECTIVITY

According to the input-output theory [73,74], the output coherent field b_{out} is the sum of the input signal b_{in} and the coherent field scattered by the qubit:

$$b_{\text{out}} = b_{\text{in}} - i\sqrt{\Gamma_r}\sigma_-(t \to \infty), \quad \text{(E1)}$$

where $\langle b_{\text{in}} \rangle = \Omega/2\sqrt{\Gamma_r}$. To calculate the reflectivity, we use Eq. (D9) with

$$r = \frac{\langle b_{\text{out}} \rangle}{\langle b_{\text{in}} \rangle} = 1 - \frac{i2\Gamma_r}{\Omega} \langle \sigma_-(t \to \infty) \rangle, \quad \text{(E2)}$$

where assuming weak drive $\Omega \ll \Gamma_1$ gives

$$r = 1 - i\Gamma_r \frac{(1 - 2\Gamma_+/\Gamma_1)}{\Delta + i\Gamma_2}. \quad \text{(E3)}$$

APPENDIX F: POWER OUTPUT

Recalling from the main text, we employ input-output theory for the output of the transmission line, where $b_{\text{in}}(t) = f_{\text{in}}(t) + \Omega/2\sqrt{\Gamma_1}$ includes the thermal noise $f_{\text{in}}(t)$ and coherent drive $\Omega/2\sqrt{\Gamma_1}$. To obtain the correct expression for the output power (and the PSD) we need to calculate correlations between the input thermal field in the waveguide and the qubit of the form $\langle \sigma_+(t) f_{\text{in}}(t') \rangle$. We can evaluate these using the result from Ref. [45], where, assuming the effect of the waveguide on the dynamics of the system obeys the standard BMS approximation, it is possible to show that for $t < t'$, the input field has not yet interacted with the qubit, so $\langle \sigma_+(t) f_{\text{in}}(t') \rangle = 0$. For $t = t'$ and $t > t'$, the thermal input can be correlated with the qubit, and the following holds:

$$\langle \sigma_+(t) f_{\text{in}}(t') \rangle = -i\sqrt{\Gamma_r} n_r \Theta(t - t') \langle \left[\sigma_+(t), \sigma_-(t')\right] \rangle \quad \text{(F1)}$$

and

$$\langle f_{\text{in}}^\dagger(t) \sigma_-(t') \rangle = i\sqrt{\Gamma_r} n_r \Theta(t' - t) \langle \left[\sigma_+(t), \sigma_-(t')\right] \rangle. \quad \text{(F2)}$$

Splitting the input field into thermal terms and coherent terms, one can evaluate the output field intensity correlator as

$$\begin{aligned} \langle b_{\text{out}}^\dagger(t) b_{\text{out}}(t') \rangle = {} & \Gamma_r (n_r + 1) \langle \sigma_+(t) \sigma_-(t') \rangle \\ & - \Gamma_r n_r \langle \sigma_-(t') \sigma_+(t) \rangle + \langle f_{\text{in}}^\dagger(t) f_{\text{in}}(t') \rangle \\ & - \frac{i\Omega^*}{2} \langle \sigma_-(t') \rangle + \frac{i\Omega}{2} \langle \sigma_+(t) \rangle + \frac{|\Omega|^2}{4\Gamma_r}. \end{aligned} \quad \text{(F3)}$$

With this we can also evaluate the equal-time terms for the power output, but it is more instructive to show the evaluation more explicitly, following the steps outlined in Ref. [75] modified to accommodate a qubit instead of cavity.

As described in the main text, we start with the full system Hamiltonian for the qubit and the two environments,

$$H_{\text{sys}} = H_q + H_r + H_n. \quad \text{(F4)}$$

The radiative (H_r) and nonradiative bath Hamiltonians (H_n) are

$$\frac{H_i}{\hbar} = \sum_k \omega_{k,i} a_{k,i}^\dagger a_{k,i} + \sum_k g_{k,i} \left(\sigma_- a_{k,i}^\dagger + \sigma_+ a_{k,i} \right), \quad \text{(F5)}$$

and include the interaction with the qubit.

First, we absorb the nonradiative bath into the qubit Hamiltonian,

$$H_q' = H_q + H_n. \quad \text{(F6)}$$

This gives us Langevin equations for the system operators coupled to the waveguide (setting $\hbar = 1$ in the following steps for simplicity),

$$\begin{aligned} \dot{\sigma}_- &= -i[\sigma_-, H_{\text{sys}}] \\ &= -i[\sigma_-, H_q'] - i[\sigma_-, \sigma_+] \sum_k g_{k,r} a_{k,r}. \end{aligned} \quad \text{(F7)}$$

We then define the spectral density for the transmission line as $J(\omega)_r = \pi \sum_k |g_{k,r}|^2 \delta(\omega - \omega_{k,r})$, insert the definition of the integral of the transmission-line modes into Eq. (F7), and make the standard Markovian approximation $J(\omega)_r = \Gamma_r$. Evaluating the result gives

$$\dot{\sigma}_- = -i[\sigma_-, H_q'] - \frac{\Gamma_r}{2}\sigma_- + i\sigma_z \sqrt{\Gamma_r} b_{\text{in}}(t). \quad \text{(F8)}$$

To obtain correlation functions between the thermal input and system operators, we omit the coherent contribution to $b_{\text{in}}(t) = f_{\text{in}}(t) + \Omega/2\sqrt{\Gamma_1}$ and multiply the equation of motion from the left first with σ_z and then with the required

system operator for the correlation function we wish to evaluate, say σ_+. Rearranging gives the form

$$i\sqrt{\Gamma_r}\langle\sigma_+ f_{\rm in}\rangle = -\langle\sigma_+\dot{\sigma}_-\rangle - \frac{\Gamma_r}{2}\langle\sigma_+\sigma_-\rangle - i\langle\sigma_+[\sigma_-, H_q']\rangle \tag{F9}$$

To evaluate the term $\langle\sigma_+\dot{\sigma}_-\rangle$ we use the formula

$$2\langle O_1 O_2\rangle = \frac{d}{dt}\langle O_1 O_2\rangle + \mathrm{Tr}\left\{\mathrm{O}_2\mathcal{L}_{\rm r}[\rho \mathrm{O}_1] - \mathrm{O}_1\mathcal{L}_{\rm r}[\mathrm{O}_2\rho]\right\}, \tag{F10}$$

where ρ is the system density matrix after tracing out the waveguide, and $\mathcal{L}_r$ is the Liouvillian describing the evolution of the system in contact with the waveguide,

$$\mathcal{L}_r[\rho] = -i[H_{\rm sys}', \rho] + \frac{\Gamma_r}{2}(n_r+1)\,\mathcal{D}[\sigma_-]\rho + \frac{\Gamma_r}{2} n_r \mathcal{D}[\sigma_+]\rho. \tag{F11}$$

Evaluating this gives

$$\langle\sigma_+\dot{\sigma}_-\rangle = -i\langle\sigma_+[\sigma_-, H_{\rm sys}']\rangle - \frac{\Gamma_r}{2}\langle\sigma_+\sigma_-\rangle - \frac{\Gamma_r n_r}{2}\langle[\sigma_+, \sigma_-]\rangle. \tag{F12}$$

Combining this with Eq. (F9), we find

$$i\sqrt{\Gamma_r}\langle\sigma_+ f_{\rm in}\rangle = \frac{\Gamma_r n_r}{2}\langle[\sigma_+, \sigma_-]\rangle. \tag{F13}$$

Performing the same steps for the other system-thermal noise correlator, and inserting into the output-power formula, we find, as expected

$$\langle b_{\rm out}^\dagger b_{\rm out}\rangle = \Gamma_r\,(n_r+1)\,\langle\sigma_+\sigma_-\rangle - \Gamma_r n_r\langle\sigma_-\sigma_+\rangle + \langle f_{\rm in}^\dagger f_{\rm in}\rangle - \frac{i\Omega^*}{2}\langle\sigma_-\rangle + \frac{i\Omega}{2}\langle\sigma_+\rangle + \frac{|\Omega|^2}{4\Gamma_r}. \tag{F14}$$

One can use this to show that the power loss $P_{\rm loss} = \hbar\omega_{01}\left(\langle b_{\rm in}^\dagger b_{\rm in}\rangle - \langle b_{\rm out}^\dagger b_{\rm out}\rangle\right)$ under zero drive ($\Omega = 0$) is given by

$$P_{\rm loss} = \frac{\hbar\omega_{01}\Gamma_r\Gamma_n(n_r - n_n)}{\Gamma_1}. \tag{F15}$$

APPENDIX G: POWER SPECTRAL DENSITY

As described in the main text, to evaluate the PSD

$$S(\omega) = \frac{\hbar\omega_{01}}{2\pi}\int_{-\infty}^{\infty} dt\, e^{-i\omega t}\langle b_{\rm out}^\dagger(t) b_{\rm out}(t')\rangle_{(t'\to\infty)} \tag{G1}$$

we need to evaluate the correlation functions contained in Eq. (F3) for the system operators. In some simple cases, this can be done by hand. For example, in the zero-drive limit, one can easily show that

$$\langle\sigma_+(t)\sigma_-(t')\rangle_{t'\to\infty} = e^{-\Gamma_2|t|}e^{-i\Delta t}\langle\sigma_+\sigma_-(t')\rangle$$

and

$$\langle\sigma_-(t')\sigma_+(t)\rangle_{t'\to\infty} = e^{-\Gamma_2|t|}e^{-i\Delta t}\langle\sigma_-\sigma_+(t')\rangle,$$

where $\langle\sigma_+\sigma_-(t')\rangle_{t'\to\infty} = \Gamma_+/\Gamma_1$ and $\langle\sigma_-\sigma_+(t')\rangle_{t'\to\infty} = \Gamma_-/\Gamma_1$. Combining these results with Eq. (6) and Eq. (G1) gives Eq. (7).

A general solution can be conveniently found by combining Eq. (D6) with the quantum regression theorem to define the two-time correlation functions, and the Fourier transform can be performed following the approach used in [46,48]. The result is cumbersome, but taking the strong-driving limit we obtain the result in Eq. (8).

APPENDIX H: THREE-LEVEL MASTER EQUATION

To evaluate the influence of higher levels in the transmon on our results, we consider a three-level master-equation model. We describe the energy difference between levels 1 and 2 with the parameter ω_{12}, such that the anharmonicity is given by $\delta/2\pi = (\omega_{12} - \omega_{01})/2\pi = -250$ MHz.

To describe the Autler-Townes splitting in the main text we apply two drives at two different frequencies, and in the rotating frame of the two-drive terms we find the system Hamiltonian to be

$$\frac{H_S}{\hbar} = (\omega_{01} - \omega_p^{(1)})|1\rangle\langle 1| + (\omega_{12} + \omega_{01} - \omega_p^{(1)} - \omega_p^{(2)})|2\rangle\langle 2| + \frac{\Omega_1}{2}\sigma_x^{(01)} + \frac{\Omega_2}{2}\sqrt{2}\sigma_x^{(12)}, \tag{H1}$$

where $\omega_p^{(i)}$ is the drive frequency of input drive i, and we define $\sigma_x^{(ij)} = |i\rangle\langle j| + |j\rangle\langle i|$, $\sigma_-^{(ij)} = |i\rangle\langle j|$, and $\sigma_+^{(ij)} = |j\rangle\langle i|$.

As we are in a regime where the anharmonicity of the qubit is larger than the decoherence rates [63], our master equation is now

$$\begin{aligned}\frac{\partial}{\partial t}\rho_S(t) = &-\frac{i}{\hbar}[H_S,\rho(t)]\\ &+\frac{\Gamma_r}{2}\left(n_r^{(01)}+1\right)\mathcal{D}[\sigma_-^{(01)}]\rho(t)+\frac{\Gamma_r}{2}n_r^{(01)}\mathcal{D}[\sigma_+^{(01)}]\rho(t)\\ &+\frac{\Gamma_n}{2}\left(n_n^{(01)}+1\right)\mathcal{D}[\sigma_-^{(01)}]\rho(t)\ +\frac{\Gamma_n}{2}n_n^{(01)}\mathcal{D}[\sigma_+^{(01)}]\rho(t)\\ &+\Gamma_r\left(n_r^{(12)}+1\right)\mathcal{D}[\sigma_-^{(12)}]\rho(t)+\Gamma_r n_r^{(12)}\mathcal{D}[\sigma_+^{(12)}]\rho(t)\\ &+\Gamma_n\left(n_n^{(12)}+1\right)\mathcal{D}[\sigma_-^{(12)}]\rho(t)+\Gamma_n n_n^{(12)}\mathcal{D}[\sigma_+^{(12)}]\rho(t)\\ &+\frac{\Gamma_\phi}{2}\sum_i\mathcal{D}[|i\rangle\langle i|]\rho(t).\end{aligned}\tag{H2}$$

The output power can be extended to consider two independent coupling operators associated with $\sigma_-^{(01)}$ and $\sigma_-^{(12)}$. Importantly, the $|1\rangle \leftrightarrow |2\rangle$ transition has a dipole moment which is $\sqrt{2}$ times larger than the $|0\rangle \leftrightarrow |1\rangle$ transition, and which enhances the coupling to the transmission line, increasing both the Rabi drive term and the dissipation rates.

For weak drives on the $|0\rangle \leftrightarrow |1\rangle$ transition alone we can observe that the main influence of the third level is to induce an additional dephasing on the qubit proportional to the thermal excitation rate from the second to the third level. To evaluate the reflectivity and power spectrum in this case, it is convenient to again work with the Heisenberg equations of motion, where in the limit of $\Omega_2 = 0$ we obtain a closed set of equations for the operators $w_1(t) = \langle\sigma_-^{(01)}(t)\rangle$, $w_1^*(t) = \langle\sigma_+^{(01)}(t)\rangle$, $w_2(t) = \langle\sigma_+^{(01)}(t)\sigma_-^{(01)}(t)\rangle$ and $w_3(t) = \langle\sigma_-^{(01)}(t)\sigma_+^{(01)}(t)\rangle$, using the normalization condition $\langle\sigma_+^{(01)}(t)\sigma_-^{(01)}(t)\rangle + \langle\sigma_-^{(01)}(t)\sigma_+^{(01)}(t)\rangle + \langle\sigma_+^{(12)}(t)\sigma_-^{(12)}(t)\rangle = 1$:

$$\frac{d}{dt}\begin{pmatrix}w_1\\ w_1^*\\ w_2\\ w_3\end{pmatrix} = M_2\begin{pmatrix}w_1\\ w_1^*\\ w_2\\ w_3\end{pmatrix} + B_2,\tag{H3}$$

where

$$M_2 = \begin{pmatrix} i\Delta-\Gamma_2^T & 0 & \frac{i\Omega_1}{2} & \frac{-i\Omega_1}{2}\\ 0 & -i\Delta-\Gamma_2^T & \frac{-i\Omega_1}{2} & \frac{i\Omega_1}{2}\\ \frac{i\Omega_1}{2} & \frac{-i\Omega_1}{2} & -\Gamma_-^{(01)}-\Gamma_1^{(12)} & \Gamma_+^{(01)}-\Gamma_-^{(12)}\\ \frac{-i\Omega_1}{2} & \frac{i\Omega_1}{2} & \Gamma_-^{(01)} & -\Gamma_+^{(01)}\end{pmatrix}$$

and

$$B_2 = \begin{pmatrix}0\\ 0\\ \Gamma_-^{(12)}\\ 0\end{pmatrix}\tag{H4}$$

and where we use $\Gamma_2^T = \Gamma_2^{(01)} + \Gamma_+^{(12)}$, indicating the added dephasing from thermalization of the $|1\rangle \leftrightarrow |2\rangle$ transition, and where $\Gamma_2^{(01)} = \Gamma_\phi + \Gamma_1^{(01)}/2$, $\Gamma_1^{(ij)} = \Gamma_+^{(ij)} + \Gamma_-^{(ij)}$, $\Gamma_+^{(ij)} = \Gamma_r n_r^{(ij)} + \Gamma_n n_n^{(ij)}$, $\Gamma_-^{(ij)} = \Gamma_r(n_r^{(ij)}+1) + \Gamma_n(n_n^{(ij)}+1)$, and $\Delta_{01} = (\omega_{01} - \omega_p^{(1)})$. Note that here we have accounted for the larger rates in the $|1\rangle \leftrightarrow |2\rangle$ transitions in Eq. (H2), hence parameters such as $\Gamma_+^{(12)}$ are just for convenience, and differ from the actual thermalization rate of the $|1\rangle \leftrightarrow |2\rangle$ transition by a factor of two.

Evaluating the reflectivity of the $|0\rangle \leftrightarrow |1\rangle$ transition with these equations, in the limit of weak drive Ω_1, gives

$$r = 1 - \frac{i\Gamma_r(1-2\Gamma_+^{(01)}/\Gamma_1^{(01)})}{\Delta + i(\Gamma_2^{(01)}+\Gamma_+^{(12)})}\mathcal{G},\tag{H5}$$

where

$$\mathcal{G} = \frac{\Gamma_-^{(12)}\Gamma_1^{(01)}}{(\Gamma_+^{(01)}\Gamma_+^{(12)}+\Gamma_-^{(12)}\Gamma_1^{(01)})} \approx 1.\tag{H6}$$

Similarly, for the output power spectrum, we can obtain the strong-drive (large Ω_1) result by generalizing the steps used in the two-level case. For the central peak, around the $|0\rangle \leftrightarrow |1\rangle$ qubit transition frequency, we find

$$S(\omega) = \frac{\hbar\omega_{01}\Gamma_r}{2\pi}\frac{\Gamma_2^T}{(\omega-\omega_{01})^2+(\Gamma_2^T)^2}\mathcal{F},\tag{H7}$$

where

$$\begin{aligned}\mathcal{F} &= \frac{\Gamma_-^{(12)}}{2\Gamma_-^{(12)}+\Gamma_+^{(12)}}\\ &= [\langle\sigma_+^{(01)}\sigma_-^{(01)}\rangle_{(t\to\infty)} = \langle\sigma_-^{(01)}\sigma_+^{(01)}\rangle_{(t\to\infty)}]_{\Omega_1\to\infty}.\end{aligned}$$

Intuitively, we see here that under a strong drive Ω_1 we still observe the added dephasing ($\Gamma_2^T = \Gamma_2^{(01)} + \Gamma_+^{(12)}$), as well as a small change in the steady-state population, on

top of the expected result from the two-level model under strong drive, which captures the thermalization with the third level.

For no drive, $\Omega_1 \to 0$, we find the thermal spectrum as

$$S(\omega) = \frac{\hbar\omega_{01}\Gamma_r}{2\pi}\frac{2\Gamma_2^T\Gamma_n\Delta n}{(\omega-\omega_{01})^2+(\Gamma_2^T)^2}\mathcal{Y}, \tag{H8}$$

where

$$\mathcal{Y} = \frac{\Gamma_-^{(12)}}{\Gamma_-^{(12)}\Gamma_1^{(01)}+\Gamma_+^{(12)}\Gamma_+^{(01)}} \tag{H9}$$

and $\Delta n = n_n^{(01)} - n_r^{(01)}$.

The side-peak contributions to the Autler-Townes data presented in the main text are based on applying a drive on the $|1\rangle \leftrightarrow |2\rangle$ while monitoring the emission from the $|0\rangle \leftrightarrow |1\rangle$ transition. We can also obtain these side peaks analytically, in a similar fashion as the above calculations. The Heisenberg equations of motion in this case, for $\Omega_1 = 0$ and $\Omega_2 \neq 0$, form a closed set of equations for the operators $z_1(t) = \langle\sigma_-^{(12)}(t)\rangle$, $z_1^*(t) = \langle\sigma_+^{(12)}(t)\rangle$, $z_2(t) = \langle\sigma_+^{(12)}(t)\sigma_-^{(12)}(t)\rangle$, $z_3(t) = \langle\sigma_-^{(12)}(t)\sigma_+^{(12)}(t)\rangle$, $z_4 = \langle\sigma_-^{(01)}(t)\rangle$, $z_4^* = \langle\sigma_+^{(01)}(t)\rangle$, $z_5 = \langle\sigma_-^{(02)}(t)\rangle$, and $z_5^* = \langle\sigma_+^{(02)}(t)\rangle$. The full equations of motion and the full result for the output spectrum are cumbersome, but evaluating the side peaks for the limit of large drive Ω_2 we find

$$S(\omega)_\pm = \frac{\hbar\omega_{01}\Gamma_r}{2\pi}\frac{2\left(\Gamma_2^T+\Gamma_2^{(02)}\right)}{4\left[\omega-\omega_{01}\pm\frac{\Omega_2}{\sqrt{2}}\right]^2+\left[\Gamma_2^T+\Gamma_2^{(02)}\right]^2} \times \frac{\Gamma_+^{(01)}+n_r^{(01)}\left[\Gamma_1^{(01)}-2\Gamma_-^{(12)}\right]}{2\left[\Gamma_-^{(12)}+\Gamma_+^{(01)}\right]-\Gamma_-^{(01)}}. \tag{H10}$$

Here we introduced a parameter which describes the dephasing rate of z_5, $\Gamma_2^{(02)} = \Gamma_\phi + \Gamma_+^{(01)}/2 + \Gamma_-^{(12)}$.

If we assume $n_n^{(01)} = n_n^{(12)}$ and $n_r^{(01)} = n_r^{(12)}$, the second term in the numerator simplifies to

$$\left(\Gamma_+^{(01)}+n_r^{(01)}\left[\Gamma_1^{(01)}-2\Gamma_-^{(12)}\right]\right) = 2\Gamma_n\Delta n. \tag{H11}$$

The various analytical results obtained in this supplementary material were checked against numerical simulations using QuTiP [68].

[1] X. Gu, A. F. Kockum, A. Miranowicz, Y.-x. Liu, and F. Nori, Microwave photonics with superconducting quantum circuits, Phys. Rep. **718**, 1 (2017).

[2] M. Kjaergaard, M. E. Schwartz, J. Braumüller, P. Krantz, J. I.-J. Wang, S. Gustavsson, and W. D. Oliver, Superconducting qubits: Current state of play, Annu. Rev. Condens. Matter Phys. **11**, 369 (2020).

[3] A. P. Place, L. V. Rodgers, P. Mundada, B. M. Smitham, M. Fitzpatrick, Z. Leng, A. Premkumar, J. Bryon, S. Sussman, and G. Cheng *et al.*, New material platform for superconducting transmon qubits with coherence times exceeding 0.3 milliseconds, Nat. Commun. **12**, 1779 (2021).

[4] A. Somoroff, Q. Ficheux, R. A. Mencia, H. Xiong, R. V. Kuzmin, and V. E. Manucharyan, Millisecond coherence in a superconducting qubit, arXiv:2103.08578 (2021).

[5] J. Lisenfeld, G. J. Grabovskij, C. Müller, J. H. Cole, G. Weiss, and A. V. Ustinov, Observation of directly interacting coherent two-level systems in an amorphous material, Nat. Commun. **6**, 6182 (2015).

[6] S. Schlör, J. Lisenfeld, C. Müller, A. Bilmes, A. Schneider, D. P. Pappas, A. V. Ustinov, and M. Weides, Correlating decoherence in transmon qubits: Low frequency noise by single fluctuators, Phys. Rev. Lett. **123**, 190502 (2019).

[7] C. Müller, J. H. Cole, and J. Lisenfeld, Towards understanding two-level-systems in amorphous solids: Insights from quantum circuits, Rep. Prog. Phys. **82**, 124501 (2019).

[8] S. Gustavsson, F. Yan, G. Catelani, J. Bylander, A. Kamal, J. Birenbaum, D. Hover, D. Rosenberg, G. Samach, and A. P. Sears *et al.*, Suppressing relaxation in superconducting qubits by quasiparticle pumping, Science **354**, 1573 (2016).

[9] G. Catelani, J. Koch, L. Frunzio, R. J. Schoelkopf, M. H. Devoret, and L. I. Glazman, Quasiparticle relaxation of superconducting qubits in the presence of flux, Phys. Rev. Lett. **106**, 077002 (2011).

[10] C. Wang, Y. Y. Gao, I. M. Pop, U. Vool, C. Axline, T. Brecht, R. W. Heeres, L. Frunzio, M. H. Devoret, and G. Catelani *et al.*, Measurement and control of quasiparticle dynamics in a superconducting qubit, Nat. Commun. **5**, 5836 (2014).

[11] S. de Graaf, L. Faoro, L. Ioffe, S. Mahashabde, J. Burnett, T. Lindström, S. Kubatkin, A. Danilov, and A. Y. Tzalenchuk, Two-level systems in superconducting quantum devices due to trapped quasiparticles, Sci. Adv. **6**, eabc5055 (2020).

[12] X. Jin, A. Kamal, A. Sears, T. Gudmundsen, D. Hover, J. Miloshi, R. Slattery, F. Yan, J. Yoder, and T. Orlando *et al.*, Thermal and residual excited-state population in a 3D transmon qubit, Phys. Rev. Lett. **114**, 240501 (2015).

[13] J. Wenner, Y. Yin, E. Lucero, R. Barends, Y. Chen, B. Chiaro, J. Kelly, M. Lenander, M. Mariantoni, A. Megrant, C. Neill, P. J. J. O'Malley, D. Sank, A. Vainsencher, H. Wang, T. C. White, A. N. Cleland, and J. M. Martinis, Excitation of superconducting qubits from hot nonequilibrium quasiparticles, Phys. Rev. Lett. **110**, 150502 (2013).

[14] D. Ristè, C. C. Bultink, K. W. Lehnert, and L. DiCarlo, Feedback control of a solid-state qubit using high-fidelity projective measurement, Phys. Rev. Lett. **109**, 240502 (2012).

[15] L. Cardani, F. Valenti, N. Casali, G. Catelani, T. Charpentier, M. Clemenza, I. Colantoni, A. Cruciani, L. Gironi, and L. Grünhaupt *et al.*, Reducing the impact of radioactivity on quantum circuits in a deep-underground facility, Nat. Commun. **12**, 2733 (2021).

[16] A. P. Vepsäläinen, A. H. Karamlou, J. L. Orrell, A. S. Dogra, B. Loer, F. Vasconcelos, D. K. Kim, A. J. Melville, B. M. Niedzielski, and J. L. Yoder *et al.*, Impact of ionizing radiation on superconducting qubit coherence, Nature **584**, 551 (2020).

[17] L. Grünhaupt, N. Maleeva, S. T. Skacel, M. Calvo, F. Levy-Bertrand, A. V. Ustinov, H. Rotzinger, A. Monfardini, G. Catelani, and I. M. Pop, Loss mechanisms and quasiparticle dynamics in superconducting microwave resonators made of thin-film granular aluminum, Phys. Rev. Lett. **121**, 117001 (2018).

[18] M. McEwen, D. Kafri, Z. Chen, J. Atalaya, K. Satzinger, C. Quintana, P. V. Klimov, D. Sank, C. Gidney, and A. Fowler *et al.*, Removing leakage-induced correlated errors in superconducting quantum error correction, Nat. Commun. **12**, 1761 (2021).

[19] D. Egger, M. Werninghaus, M. Ganzhorn, G. Salis, A. Fuhrer, P. Müller, and S. Filipp, Pulsed reset protocol for fixed-frequency superconducting qubits, Phys. Rev. Appl. **10**, 044030 (2018).

[20] J. Roßnagel, S. T. Dawkins, K. N. Tolazzi, O. Abah, E. Lutz, F. Schmidt-Kaler, and K. Singer, A single-atom heat engine, Science **352**, 325 (2016).

[21] J. P. Peterson, T. B. Batalhão, M. Herrera, A. M. Souza, R. S. Sarthour, I. S. Oliveira, and R. M. Serra, Experimental characterization of a spin quantum heat engine, Phys. Rev. Lett. **123**, 240601 (2019).

[22] K. Ono, S. N. Shevchenko, T. Mori, S. Moriyama, and F. Nori, Analog of a quantum heat engine using a single-spin qubit, Phys. Rev. Lett. **125**, 166802 (2020).

[23] H. T. Quan, Y.-x. Liu, C. P. Sun, and F. Nori, Quantum thermodynamic cycles and quantum heat engines, Phys. Rev. E **76**, 031105 (2007).

[24] G. Maslennikov, S. Ding, R. Hablützel, J. Gan, A. Roulet, S. Nimmrichter, J. Dai, V. Scarani, and D. Matsukevich, Quantum absorption refrigerator with trapped ions, Nat. Commun. **10**, 202 (2019).

[25] M. Xu, X. Han, C.-L. Zou, W. Fu, Y. Xu, C. Zhong, L. Jiang, and H. X. Tang, Radiative cooling of a superconducting resonator, Phys. Rev. Lett. **124**, 033602 (2020).

[26] W. Schoonveld, J. Wildeman, D. Fichou, P. Bobbert, B. Van Wees, and T. Klapwijk, Coulomb-blockade transport in single-crystal organic thin-film transistors, Nature **404**, 977 (2000).

[27] K. Schwab, E. Henriksen, J. Worlock, and M. L. Roukes, Measurement of the quantum of thermal conductance, Nature **404**, 974 (2000).

[28] C. W. Chang, D. Okawa, A. Majumdar, and A. Zettl, Solid-state thermal rectifier, Science **314**, 1121 (2006).

[29] M. Partanen, K. Y. Tan, J. Govenius, R. E. Lake, M. K. Mäkelä, T. Tanttu, and M. Möttönen, Quantum-limited heat conduction over macroscopic distances, Nat. Phys. **12**, 460 (2016).

[30] M. Meschke, W. Guichard, and J. P. Pekola, Single-mode heat conduction by photons, Nature **444**, 187 (2006).

[31] H. T. Quan, Y. D. Wang, Y. X. Liu, C. P. Sun, and F. Nori, Maxwell's demon assisted thermodynamic cycle in superconducting quantum circuits, Phys. Rev. Lett. **97**, 180402 (2006).

[32] M. Naghiloo, D. Tan, P. Harrington, J. Alonso, E. Lutz, A. Romito, and K. Murch, Heat and work along individual trajectories of a quantum bit, Phys. Rev. Lett. **124**, 110604 (2020).

[33] N. Cottet, S. Jezouin, L. Bretheau, P. Campagne-Ibarcq, Q. Ficheux, J. Anders, A. Auffèves, R. Azouit, P. Rouchon, and B. Huard, Observing a quantum Maxwell demon at work, Proc. Natl. Acad. Sci. **114**, 7561 (2017).

[34] J. Senior, A. Gubaydullin, B. Karimi, J. T. Peltonen, J. Ankerhold, and J. P. Pekola, Heat rectification via a superconducting artificial atom, Commun. Phys. **3**, 40 (2020).

[35] C. Cherubim, F. Brito, and S. Deffner, Non-thermal quantum engine in transmon qubits, Entropy **21**, 545 (2019).

[36] A. Ronzani, B. Karimi, J. Senior, Y.-C. Chang, J. T. Peltonen, C. Chen, and J. P. Pekola, Tunable photonic heat transport in a quantum heat valve, Nat. Phys. **14**, 991 (2018).

[37] D. Roy, C. M. Wilson, and O. Firstenberg, Colloquium: Strongly interacting photons in one-dimensional continuum, Rev. Mod. Phys. **89**, 021001 (2017).

[38] A. F. Kockum and F. Nori, Quantum bits with Josephson junctions, in F. Tafuri (ed.) Fundamentals and Frontiers of the Josephson Effect. (Springer Series in Materials Science, vol 286., 2019) p. 703.

[39] J. Monsel, M. Fellous-Asiani, B. Huard, and A. Auffèves, The energetic cost of work extraction, Phys. Rev. Lett. **124**, 130601 (2020).

[40] H.-P. Breuer and F. Petruccione, *The Theory of Open Quantum Systems* (Oxford University Press, Oxford, England, 2002).

[41] J. Koch, T. M. Yu, J. Gambetta, A. A. Houck, D. I. Schuster, J. Majer, A. Blais, M. H. Devoret, S. M. Girvin, and R. J. Schoelkopf, Charge-insensitive qubit design derived from the Cooper pair box, Phys. Rev. A **76**, 042319 (2007).

[42] I.-C. Hoi, A. F. Kockum, L. Tornberg, A. Pourkabirian, G. Johansson, P. Delsing, and C. Wilson, Probing the quantum vacuum with an artificial atom in front of a mirror, Nat. Phys. **11**, 1045 (2015).

[43] P. Y. Wen, A. F. Kockum, H. Ian, J. C. Chen, F. Nori, and I.-C. Hoi, Reflective amplification without population inversion from a strongly driven superconducting qubit, Phys. Rev. Lett. **120**, 063603 (2018).

[44] Y. Lu, I. Strandberg, F. Quijandría, G. Johansson, S. Gasparinetti, and P. Delsing, Propagating Wigner-negative states generated from the steady-state emission of a superconducting qubit, Phys. Rev. Lett. **126**, 253602 (2021).

[45] Crispin Gardiner and Peter Zoller, *Quantum Noise: A Handbook of Markovian and non-Markovian Quantum Stochastic Methods with Applications to Quantum Optics* (Springer Science, Berlin, Heidelberg, 2004), Vol. 56.

[46] K. Koshino and Y. Nakamura, Control of the radiative level shift and linewidth of a superconducting artificial atom through a variable boundary condition, New J. Phys. **14**, 043005 (2012).

[47] O. Astafiev, A. M. Zagoskin, A. Abdumalikov, Y. A. Pashkin, T. Yamamoto, K. Inomata, Y. Nakamura, and J. S. Tsai, Resonance fluorescence of a single artificial atom, Science **327**, 840 (2010).

[48] Y. Lu, A. Bengtsson, J. J. Burnett, E. Wiegand, B. Suri, P. Krantz, A. F. Roudsari, A. F. Kockum, S. Gasparinetti, G. Johansson, and P. Delsing, Characterizing decoherence rates of a superconducting qubit by direct microwave scattering, Npj Quantum Inf. **7**, 35 (2021).

[49] S. H. Autler and C. H. Townes, Stark effect in rapidly varying fields, Phys. Rev. **100**, 703 (1955).

[50] F. W. J. Hekking and J. P. Pekola, Quantum jump approach for work and dissipation in a two-level system, Phys. Rev. Lett. **111**, 093602 (2013).

[51] C. Elouard, D. H. Martí, M. Esposito, and A. Auffèves, Thermodynamics of optical Bloch equations, New J. Phys. **22**, 103039 (2020).

[52] K. Funo, M. Ueda, and M. Sagawa, Quantum Fluctuation Theorems, in Binder F., Correa L., Gogolin C., Anders J., and Adesso G. (eds.) Thermodynamics in the Quantum Regime. Fundamental Theories of Physics. (Springer Series in Materials Science, vol. 195, 2018) p. 249.

[53] J. Wenner, Y. Yin, E. Lucero, R. Barends, Y. Chen, B. Chiaro, J. Kelly, M. Lenander, M. Mariantoni, and A. Megrant *et al.*, Excitation of superconducting qubits from hot nonequilibrium quasiparticles, Phys. Rev. Lett. **110**, 150502 (2013).

[54] K. Serniak, M. Hays, G. De Lange, S. Diamond, S. Shankar, L. Burkhart, L. Frunzio, M. Houzet, and M. Devoret, Hot nonequilibrium quasiparticles in transmon qubits, Phys. Rev. Lett. **121**, 157701 (2018).

[55] W. D. Oliver and P. B. Welander, Materials in superconducting quantum bits, MRS Bulletin **38**, 816 (2013).

[56] J. Schleeh, J. Mateos, I. Íñiguez-de-la-Torre, N. Wadefalk, P. A. Nilsson, J. Grahn, and A. J. Minnich, Phonon black-body radiation limit for heat dissipation in electronics, Nat. Mater. **14**, 187 (2015).

[57] Z. H. Peng, S. E. De Graaf, J. S. Tsai, and O. V. Astafiev, Tuneable on-demand single-photon source in the microwave range, Nat. Commun. **7**, 12588 (2016).

[58] Y. Zhou, Z. H. Peng, Y. Horiuchi, O. V. Astafiev, and J. S. Tsai, Tunable microwave single-photon source based on transmon qubit with high efficiency, Phys. Rev. Appl. **13**, 034007 (2020).

[59] X. You, A. A. Clerk, and J. Koch, Positive-and negative-frequency noise from an ensemble of two-level fluctuators, Phys. Rev. Res. **3**, 013045 (2021).

[60] L. Spietz, K. Lehnert, I. Siddiqi, and R. Schoelkopf, Primary electronic thermometry using the shot noise of a tunnel junction, Science **300**, 1929 (2003).

[61] L. Wang, O.-P. Saira, and J. Pekola, Fast thermometry with a proximity Josephson junction, Appl. Phys. Lett. **112**, 013105 (2018).

[62] Z. Wang, M. Xu, X. Han, W. Fu, S. Puri, S. M. Girvin, H. X. Tang, S. Shankar, and M. H. Devoret, Quantum microwave radiometry with a superconducting qubit, Phys. Rev. Lett. **126**, 180501 (2021).

[63] M. Scigliuzzo, A. Bengtsson, J.-C. Besse, A. Wallraff, P. Delsing, and S. Gasparinetti, Primary thermometry of propagating microwaves in the quantum regime, Phys. Rev. X **10**, 041054 (2020).

[64] B. Albanese, S. Probst, V. Ranjan, C. W. Zollitsch, M. Pechal, A. Wallraff, J. J. Morton, D. Vion, D. Esteve, and E. Flurin *et al.*, Radiative cooling of a spin ensemble, Nat. Phys. **16**, 751 (2020).

[65] M. Mirhosseini, A. Sipahigil, M. Kalaee, and O. Painter, Superconducting qubit to optical photon transduction, Nature **588**, 599 (2020).

[66] W. Hease, A. Rueda, R. Sahu, M. Wulf, G. Arnold, H. G. Schwefel, and J. M. Fink, Bidirectional electro-optic wavelength conversion in the quantum ground state, PRX Quantum **1**, 020315 (2020).

[67] X. Han, W. Fu, C. Zhong, C.-L. Zou, Y. Xu, A. Al Sayem, M. Xu, S. Wang, R. Cheng, and L. Jiang *et al.*, Cavity piezo-mechanics for superconducting-nanophotonic quantum interface, Nat. Commun. **11**, 3237 (2020).

[68] J. Johansson, P. Nation, and F. Nori, QuTiP 2: A Python framework for the dynamics of open quantum systems, Comput. Phys. Commun. **184**, 1234 (2013).

[69] P. Welch, The use of fast Fourier transform for the estimation of power spectra: A method based on time averaging over short, modified periodograms, IEEE Trans. Audio Electroacoustics **15**, 70 (1967).

[70] R. Barends, J. Wenner, M. Lenander, Y. Chen, R. C. Bialczak, J. Kelly, E. Lucero, P. O'Malley, M. Mariantoni, and D. Sank *et al.*, Minimizing quasiparticle generation from stray infrared light in superconducting quantum circuits, Appl. Phys. Lett. **99**, 113507 (2011).

[71] T. Tai, J.-N. Cai, and S. M. Anlage, Coherence Time Enhancement of Interacting Two-Level Systems in Aluminum Superconducting Resonators, arXiv:2109.11742 (2021).

[72] S. Krinner, S. Storz, P. Kurpiers, P. Magnard, J. Heinsoo, R. Keller, J. Lütolf, C. Eichler, and A. Wallraff, Engineering cryogenic setups for 100-qubit scale superconducting circuit systems, EPJ Quantum Technol. **6**, 2 (2019).

[73] B. Yurke and J. S. Denker, Quantum network theory, Phys. Rev. A **29**, 1419 (1984).

[74] C. W. Gardiner and M. J. Collett, Input and output in damped quantum systems, Phys. Rev. A **31**, 3761 (1985).

[75] H. J. Carmichael, *Statistical Methods in Quantum Optics 1* (Springer-Verlag, Berlin, Heidelberg, 1999).